Simple shear deformation and quartz crystallographic fabrics: a possible natural example from the Torridon area of NW Scotland

R. D. Law

Department of Geological Sciences, Virginia Polytechnic Institute & State University, Blacksburg, VA 24061, U.S.A.

S. M. Schmid

Geologisches Institut, ETH—Zentrum, Zurich CH 8092, Switzerland

and

J. Wheeler

Department of Geological Sciences, University of Liverpool, Liverpool L69 3BX, U.K.

Abstract—In this paper the microstructures and crystallographic fabrics of a 30 cm wide deformed quartz vein from the Torridon area of NW Scotland are described. The vein, which lies along a joint separating two blocks of Proterozoic gneiss, was deformed by crystal–plastic processes when the rigid joint blocks moved in opposite directions parallel to the vein margins. Mylonitic foliation within this quartzose ductile shear zone locally displays the classic orientation variation expected for heterogeneous simple shear deformation.

In thin section the vein is a mylonite composed of dynamically recrystallized, elongate quartz grains aligned oblique to the mylonitic foliation. Fabrics within the central part of the vein have been examined by optical and X-ray texture goniometry methods, together with Orientation Distribution Function (ODF) analysis.

The a-axis fabric consists of a dominant single point maximum, orientated within the XZ plane at 9° to the lineation (X); this point maximum occupies a pole position to the corresponding single girdle c-axis fabric. For individual positions on the c-axis fabric skeleton, the orientations of potential crystallographic slip systems (slip plane and direction) relative to shear zone co-ordinates have been calculated by ODF analysis. The calculation of *relative resolved shear stresses* (*Schmid factors*) for the potential slip systems, assuming a simple shear kinematic framework, reveals an elegantly simple relationship between individual grain c-axis orientation and corresponding orientations of potential slip systems. These results are readily interpreted in terms of bulk simple shear deformation.

INTRODUCTION

Simple shear is commonly assumed to be the dominant strain path within mylonite zones. Strain paths involving progressive heterogeneous simple shear present particularly attractive interpretative solutions to deformation zones because strain compatibility is maintained in a very simple way. Geometrical relationships between tectonic foliation, lineation and shear zone boundaries with increasing heterogeneous shear strain have been examined from a theoretical viewpoint by Ramsay & Graham (1970) and reviewed by Ramsay (1980).

In principle, the analysis of crystallographic preferred orientation (referred to as fabrics in this paper) within mylonites is of considerable interest to the structural geologist because fabric development is controlled by: (1) the active deformation mechanisms (i.e. the active slip systems); (2) the magnitude and symmetry of finite strain; and, (3) the strain path or kinematic framework (see brief review by Schmid 1982). The influence of these factors on fabric development has been demonstrated by experimental studies (e.g. Tullis *et al.* 1973, Dell'Angelo & Tullis in press) and computer simulations

of fabric development in quartz during plastic deformation, based on the Taylor–Bishop–Hill model by Lister and co-workers (Lister *et al.* 1978, Lister & Paterson 1979, Lister & Hobbs 1980). It should, in principle, be possible to deduce the role of each factor during deformation on the basis of measured fabrics. However, what makes the interpretation of natural fabrics difficult is that all these factors contribute together to the final fabric pattern and it is extremely difficult to isolate the influence of individual factors.

Fabrics within natural ductile (crystal–plastic) shear zones have received particularly intense study (e.g. see reviews by Lister & Williams 1979 and more recently Schmid & Casey 1986). This is not surprising since, if deformation in such zones is by progressive heterogeneous simple shear, then strain path and strain symmetry are known, thus enabling the relationship between active deformation mechanisms and fabrics to be studied in isolation from other geological factors. For quartz-rich tectonites the asymmetrical relationships predicted by theoretical studies (e.g. Etchecopar 1977, Lister & Hobbs 1980, Etchecopar & Vasseur 1987) between c-axis and a-axis fabrics and finite strain fea-

tures (foliation and lineation) are commonly observed in natural shear zones (e.g. see review by Bouchez *et al.* 1983) and appear, in general, to constitute reliable shear sense indicators.

A strict relationship between fabric evolution and the kinematic framework associated with simple shear was initially suggested by the fabric simulation work of Etchecopar (1977). Following this simulation work it has been proposed (e.g. Bouchez 1978, Burg & Laurent 1978, Bouchez *et al.* 1979) that in simple shear deformation of quartz rich rocks, the dominant crystallographic slip direction $\langle a \rangle$ within individual quartz grains will tend to become aligned parallel to the direction of bulk simple shear deformation. Thus, for simple shear deformation, the dominant a-axis point maximum would be interpreted as indicating the shear direction and, with increasing shear strain, one would expect the lineation (X) lying within the foliation (XY) to be progressively rotated into alignment with the shear direction parallel a-axis maximum (Burg & Laurent 1978, fig. 14). This dominant a-axis point maximum should occupy a pole position to an associated straight single girdle distribution of c-axes (Etchecopar 1977). At very high shear strains, therefore, it would be predicted that the dominant a-axis point maximum should lie within the XZ plane at a very low angle to X, whilst the associated single girdle c-axis fabric would be orientated sub-perpendicular to X.

Measurements of natural shear zone tectonites by Burg & Laurent (1978), Simpson (1981, specimen R405) and Schmid & Casey (1986, but only specimens CC1 and R405) support this simple model. However, within many mylonite zones containing quartz tectonites characterized by single girdle c-axis fabrics, the angle between the dominant a-axis point maximum and the lineation is too large (i.e. the predicted shear strain is too small) when compared with predictions from field relationships (see discussion by Mancktelow 1987). For example, Law *et al.* (1986) and Law (1987) have described quartz mylonites very close to the Moine Thrust (NW Scotland) where the foliation is effectively parallel to the thrust surface, but the dominant a-axis point maximum still lies at an angle of 20–30° to the lineation. Such observations must bring into question the general applicability of Etchecopar's attractively simple model.

One possible interpretation of these observations is that deformation has involved bulk simple shear, but that the detailed crystallographic slip model proposed by Etchecopar (1977) is not strictly applicable to natural deformation (Mancktelow 1987). A second, geologically more important, interpretation is that deformation has significantly departed from simple shear. For example, Law *et al.* (1984, 1986) and Platt & Behrmann (1986) proposed, on the basis of microstructural and textural criteria, that deformation associated with mylonite formation in the Moine thrust zone and Betic Cordilleras may have involved a significant component of coaxial deformation. For mylonites from the Betic Cordilleras, Platt & Behrmann (1986) found that deformation was essentially plane strain. In contrast, recent

work in the Moine thrust zone has led Law (1987) to suggest that mylonite formation may have been locally associated with heterogeneous deformation involving a component of flattening strain.

These observations should warn us not to assume that mylonites within shear zones always develop by strict bulk simple shear. In this paper we look at the problem from an alternative viewpoint. If a natural shear zone displayed the classic geometrical relationships between finite strain features and shear zone boundaries predicted by Ramsay & Graham (1970), then crystallographic fabrics within such a shear zone should be readily interpretable in terms of simple shear deformation, if both the bulk simple shear and crystallographic slip models (such as the Etchecopar 1977, 1986 models) are applicable. One such shear zone was found in the Torridon area of NW Scotland and forms the subject of this paper.

DESCRIPTION OF SHEAR ZONE

A 30 cm wide deformed planar quartz vein was found (grid reference NG 840 530) at the head of Upper Loch Torridon (NW Scotland). The vein, which lies along a joint separating two blocks of Proterozoic gneiss (Wheeler 1986), was deformed by crystal–plastic processes when the rigid joint blocks moved in opposite directions parallel to the vein margins. Mylonitic foliation within this shear zone locally displays the orientation variation expected (Ramsay & Graham 1970) for heterogeneous simple shear deformation (Fig. 1a).

The orthogonal reference system used in this paper is defined as the Z axis being perpendicular to the foliation, and the Y axis lying within the foliation and being perpendicular to the lineation (X). Use of X, Y and Z in the following discussion refers to this co-ordinate system and does not implicitly assume a parallelism with the finite strain axes.

In hand specimen the margins of the deformed quartz vein are commonly marked by a 2.5 cm wide zone of coarsely crystalline quartz and feldspar. The central part of the vein is composed of translucent quartz (with subordinate feldspar) and displays an intensely developed foliation and lineation (Fig. 1). On polished XZ surfaces of specimen T2, cut parallel to the lineation and perpendicular to the vein walls, foliation at the margins of the translucent zone is orientated at 45° (±3°) to the vein walls. Traced over a distance of 1 cm perpendicular to the vein walls towards the vein centre, this foliation curves over into sub-parallelism with the vein walls (Fig. 1a). Within specimen T2 the minimum recorded angle in XZ sections between mylonitic foliation and quartz vein boundaries is 6°.

In the central part of the quartz vein, the mylonitic foliation strikes 160° and dips at 66°W. Lineation plunges at 12° towards 334°. The curved trajectory of mylonitic foliation (as exposed on the XZ section and viewed upwards along the Y axis) traced into the centre of the sheared quartz vein is consistent with the more
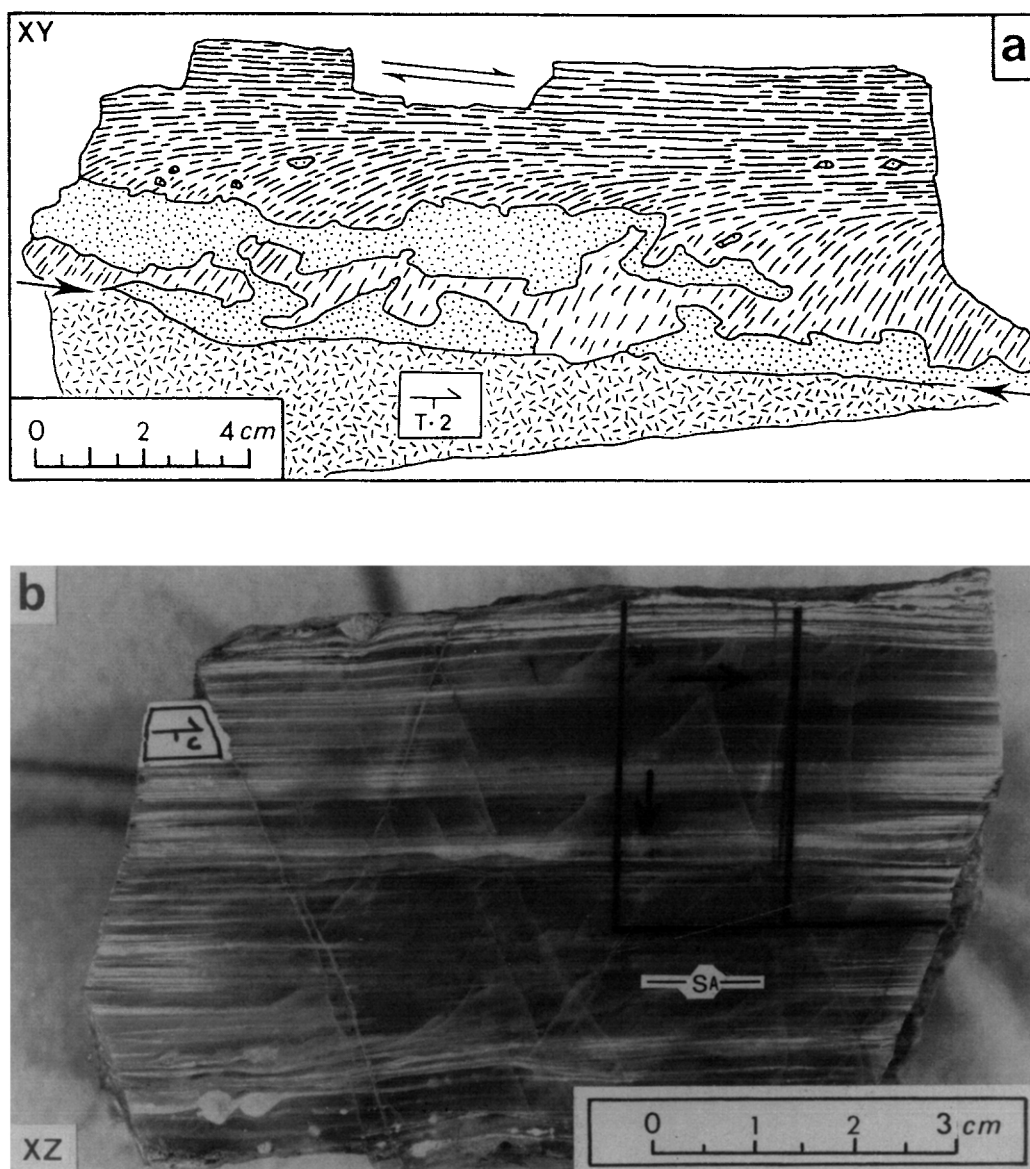
Fig. 1. (a) Tracing of XZ section cut from specimen T2. Wallrock composed of Proterozoic gneiss (cross-hatch ornament), vein composed of non-foliated pink feldspar domains (stipple ornament) and foliated quartz. Shear zone boundary (position indicated by heavy arrows) taken as junction between wallrock and vein material. Note mylonitic foliation within quartz vein curving towards parallelism with shear zone boundary and indicating a dextral shear sense. Foliation intensity (represented by foliation spacing) increases away from shear zone boundary. (b) XZ section of specimen T1 (from centre of shear zone) displaying intense mylonitic foliation (S_A). Position of petrofabrics slab indicated. Sections in both (a) and (b) viewed towards the ENE.
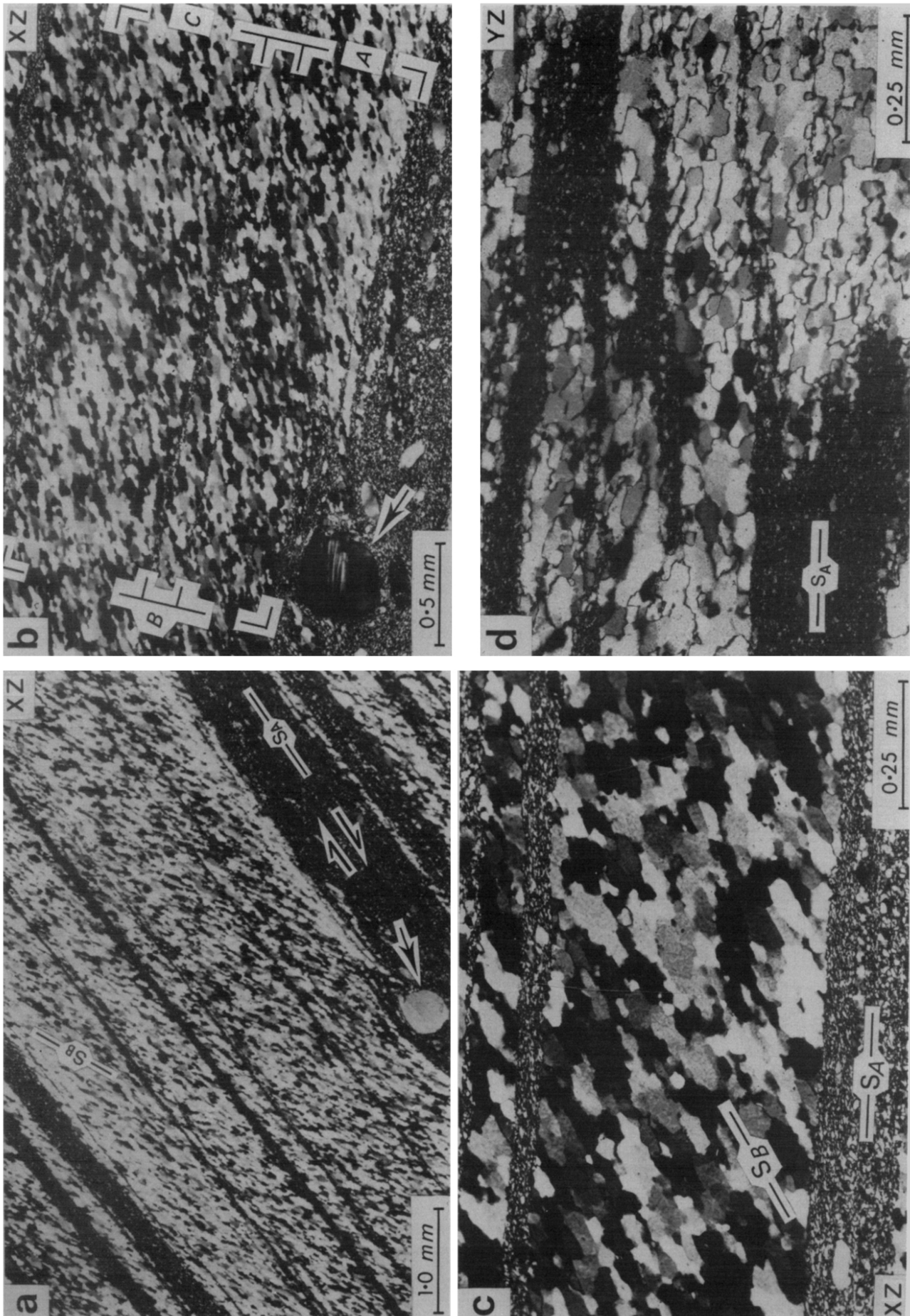
westerly joint block overlying the quartz vein moving towards the SSE. This inferred shear sense is in agreement with all microstructures and crystallographic fabrics recorded, and is indicated in the present paper by a dextral shear sense.

On polished hand specimen surfaces of specimen T1, taken from the centre of the shear zone, mylonitic foliation is picked out by planar domains of translucent quartz 1 mm–1 cm in width, separated by pink-coloured domains predominantly composed of extremely fine-grained feldspar that are occasionally observed to form tails on large (3–5 mm) feldspar porphyroclasts (Fig. 1b). No folding of the mylonitic foliation has been observed on any of the XZ polished sections examined. However, in YZ sections (specimen T1) cut from the centre of the deformed quartz vein, foliation is observed to be intensely contorted and to anastomose in a complex manner.

Microstructures

In XZ thin sections the deformed quartz vein is seen to be a classic Type II S–C mylonite in the sense of Lister & Snoke (1984). Two planar domain types, A and B, aligned parallel to the macroscopic mylonitic foliation (S_A) may be distinguished (Figs. 2a–c). Type A domains are composed of fairly equant fine-grained (<5 μm) feldspar and quartz; individual grains can rarely be resolved with the optical microscope. These domains range in width from 20 to 600 μm (Figs. 2a & c), the thinner domains being more common. Large feldspar porphyroclasts with fine-grained feldspar rich tails are occasionally observed in the thicker domains (Figs. 2a & b).

Type B domains, which are volumetrically the more important, are composed of dynamically recrystallized quartz grains and range from 40 to 700 μm in width (Fig. 2). Individual quartz grains in these domains are commonly elongate displaying, in XZ thin sections, aspect ratios ranging from 2:1 to 5:1. Typical long and short dimensions of these grains are 110 and 35 μm, respectively. Grain long axes are ubiquitously orientated oblique to domain boundaries, the angle of obliquity locally ranging from 18 to 36°. Such quartz-rich domains have probably undergone many cycles of dynamic recrystallization (Means 1981, Lister & Snoke 1984, Knipe & Law 1987). Following the terminology of Law *et al.* (1984) the preferred grain shape alignment observed within Type B domains will be referred to as S_B. The consistent sense of obliquity between grain shape alignment S_B and mylonitic foliation S_A (Fig. 2) yields the same shear sense as that indicated by macroscopic shear

zone geometry (Fig. 1) and asymmetrical quartz crystallographic fabrics.

In YZ sections recrystallized quartz grains in Type B domains are generally more equant than in XZ sections with aspect ratios ranging from 1:1 to 2:1 and grain long axes are orientated sub-parallel to domain boundaries. In YZ sections, Type A domains are commonly either lenticular, anastomosing or irregular in outline (Fig. 2d).

Because the active deformation mechanism within this sheared vein is intracrystalline plasticity, it is argued that the related quartz crystallographic fabrics described below must be associated with a constant volume deformation. Microstructures, including foliation patterns, and crystallographic fabrics within the vein are indicative of strongly non-coaxial, essentially plane strain deformation. It is therefore argued that this crystal-plastic deformation component must have closely approximated to simple shear.

TECHNIQUES OF PETROFABRIC ANALYSIS

A single specimen (T1) collected from the centre of the quartz vein was selected for detailed analysis. From this specimen, in which foliation (viewed in XZ sections) remains in a constant orientation, a small block (3.2 × 1.8 cm) was cut and polished such that the XZ face to be measured was perpendicular to foliation and parallel to lineation—see Fig. 1(b).

X-ray texture goniometry was carried out at ETH—Zurich. The specimen block was mounted on the texture goniometer in an orientation such that scanning occurred perpendicular to the foliation. The scan distance was approximately 14 mm. For complete analysis, nine crystallographic planes were measured in combined reflection and transmission modes following the methods of Schmid *et al.* (1981) and Casey (1981), with a total measuring time of approximately 1 week. The Orientation Distribution Function (ODF) was calculated, and sections through the ODF, regenerated pole figures and inverse pole figures were plotted using the computer program package of Casey (1981).

On completion of the goniometry measurements, a thin section was taken for optical study from the face of the reflection scan block. Domainal variation in quartz c-axis preferred orientation within this section was studied using an optical microscope and universal stage. Three adjacent quartz-rich domains (A, B and C) in this block (Fig. 1b) were selected for detailed analysis. A further two sampling areas (1 and 2) were selected from quartz-rich domains located immediately to the right of

---

Fig. 2. (a–c) XZ sections of specimen T1 petrofabrics slab. All XZ sections viewed towards the ENE. Note distribution of Type A (dark, fine-grained) and B (coarse-grained, quartz-rich) domains. Mylonitic foliation (S_A) defined by boundaries between domains is oblique to quartz grain shape alignment (S_B) in Type B domains indicating a dextral shear sense. Location of petrofabrics measuring areas A, B and C indicated in (b). Feldspar grain within Type A domain common to (a) and (b) is arrowed. (c) Detail of quartz grain shape alignment (S_B) in Type B domain. (d) YZ section of specimen T1. Note anastomosing nature of Type A and B domains, and preferred alignment of grain long axes sub-parallel to planar segments of domain boundaries (S_A) within the quartz-rich Type B domains.

the reflection scan block (Fig. 1b). The locations of sampling areas A, B and C are shown in Fig. 2(b). Within each pre-designated sampling area, all individual quartz grains were measured. This analysis was facilitated by mapping the locations of individual grains on a photomicrograph mosaic during universal stage work.

All petrofabric data are presented on equal-area, upper-hemisphere stereographic projections whose plane of projection contains the specimen lineation and pole to foliation. In all projections (except Figs. 5 and 7) the foliation is vertical and lineation lying within the foliation is horizontal. Both stereograms and micrographs are geographically viewed upwards towards the ENE.

CRYSTALLOGRAPHIC FABRICS

Optically measured c-axis fabrics

Quartz c-axis fabrics from the five sampling areas selected for detailed analysis within Type B domains are shown in Fig. 3. All are essentially single girdle fabrics,

containing the specimen Y axis and passing through the XZ plane at approximately 8° to the pole (Z) to mylonitic foliation (S_A). A composite c-axis fabric produced by combining the individual fabrics from the five sampling areas is also shown in Fig. 3.

Two dominant clusterings (point maxima) of c-axes are present in each measured fabric. These maxima are inclined within the single girdle fabric at approximately 72° ('*upper*' maximum in each fabric shown in Fig. 3) and 62° ('*lower*' maximum) to the specimen Y axis (Fig. 3). In detail the individual c-axis single girdle fabric skeletons are slightly kinked, the central segment of each girdle, located between the two point maxima and passing through Y, being orientated at 2–3° to the specimen YZ plane, whilst the peripheral girdle segment is orientated at 7–10° to the YZ plane. This is interesting since the pole to the bulk shear plane (inferred from shear zone geometry) bisects the acute angle between the central and peripheral girdle segments.

The asymmetry of c-axis fabrics with respect to specimen co-ordinates indicates a dextral shear sense in agreement with the observed obliquity between S_A and S_B.
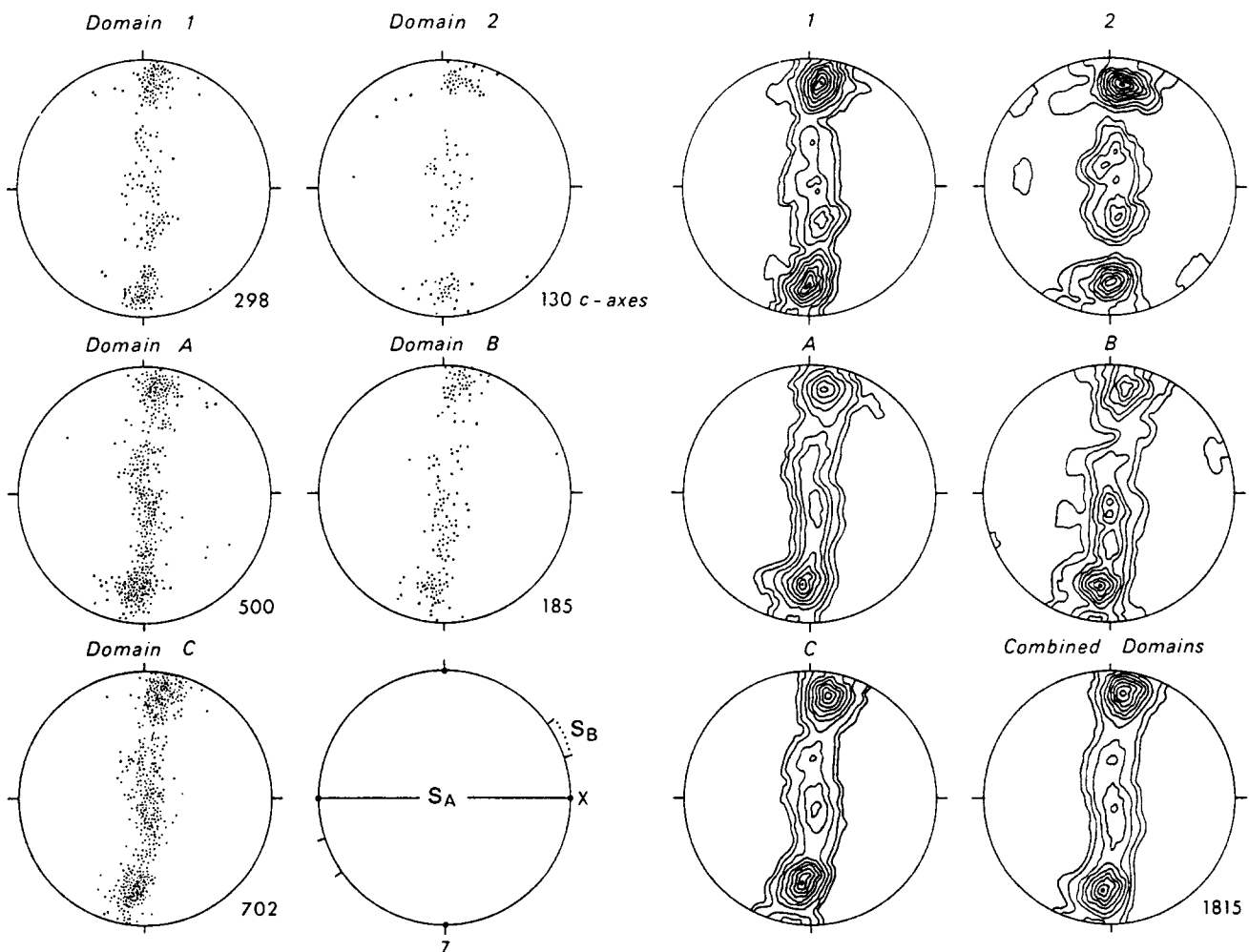

Fig. 3. Optically measured quartz c-axis fabrics within five Type B domains from specimen T1; micrograph of domains A, B and C shown in Fig. 2(b). Number of grains (c-axis) measured in each domain indicated. Composite fabric from the five combined domains also shown. Contour intervals: 0.5, 1, 3, 5, 7, 10, 12, 15, 17, 20 times uniform distribution. Orientation of mylonitic foliation (S_A), lineation (X), pole to mylonitic foliation (Z) and range of dynamically recrystallized quartz grain shape alignment (S_B) indicated. All upper-hemisphere, equal-area projections viewed upwards towards the ENE.
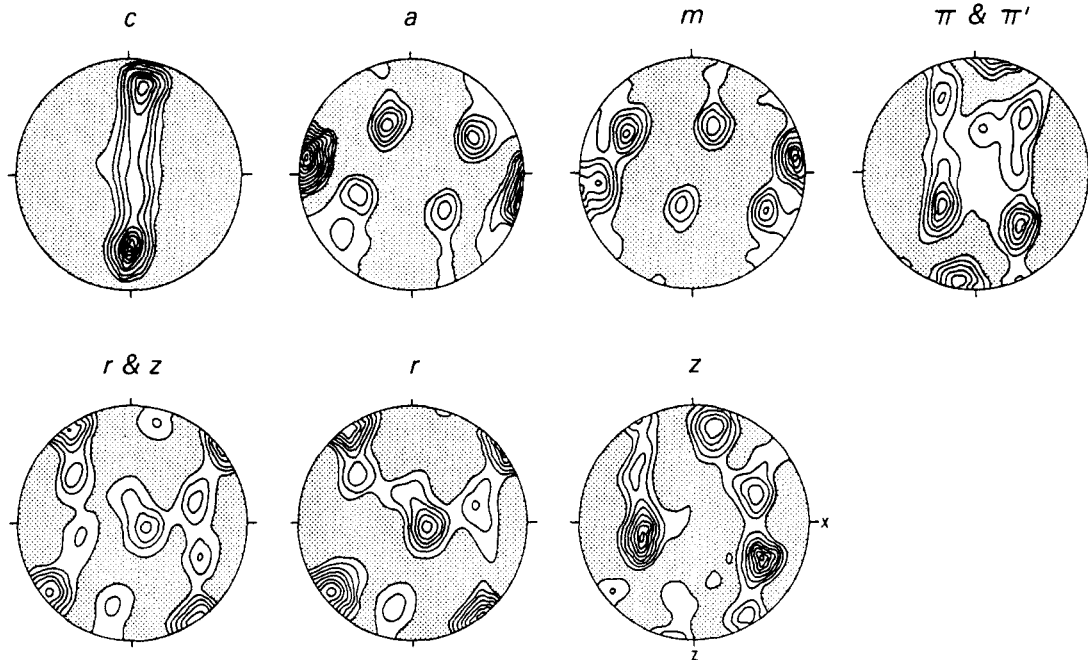
c   a   m   π & π'

r & z   r   z

Fig. 4. Crystallographic fabrics calculated from the ODF for specimen T1. Pole figures include: c-axis, second-order prism (a), first-order prism (m), combined positive and negative acute rhombs (π and π'), combined positive and negative rhombs (r and z), positive rhombs (r) and negative rhombs (z). Contour intervals for calculated c-axis pole figure: 1, 2, 3, ..., 7, 8, 9 times uniform distribution. Contour intervals for all other pole figures: 1.0, 1.5, 2.0, ..., 6.5, 7.0, 7.5 times uniform distribution. Less than uniform distribution stippled. Orientation convention as in Fig. 3. All upper-hemisphere, equal-area projections viewed upwards towards the ENE.

Fabrics measured by X-ray texture goniometry

Regenerated pole figures (calculated from the ODF) for specimen T1 are shown in Fig. 4. It should be emphasized that these pole figures, although containing data from the areas studied optically, were obtained by scanning over a much larger aggregate of grains than could, in practice, be measured by optical methods. Angular relationships between the crystal directions studied by X-ray texture goniometry are indicated in Fig. 5.

A good correlation is found between the optically measured and regenerated skeletal c-axis pole figures (cf. Figs. 3 and 4). The regenerated c-axis pole figures consist of a single girdle fabric which is orientated at approximately 9° to the specimen YZ plane and contains the Y direction (Fig. 4). Two prominent point maxima are present within this single girdle: whilst the 'upper' c-axis maximum (7.5 times uniform distribution) is orientated at 65° to the specimen Y direction (cf. 72° in optically measured fabric), the 'lower' maximum (9.9 times uniform distribution) is orientated at 55° to the Y direction (62° in optical fabric).

The regenerated second-order prism (a-axis) pole figure consists of five point maxima arranged on two great circles to which the two point maxima in the regenerated c-axis fabric occupy pole positions. These two great circles intersect in the XZ plane at 9° to the lineation, the most intense a-axis maximum (7.7 times uniform distribution) being coincident with this intersection position (Fig. 4). The corresponding regenerated first order prism (m-axis) pole figure consists of six point maxima, also aligned within these great circles and, as

dictated by crystallography, orientated at 30° to the a-axis maxima. The regenerated positive (r) and negative (z) rhomb pole figures are completely separated.

Analysis of the pole figures reproduced in Fig. 4 clearly indicates that the bulk crystallographic fabric of specimen T1 essentially consists of two single crystal orientations, whose c-axes coincide with the two c-axis point maxima. The pole figures further indicate that only one crystal orientation about each of these c-axis positions (placing a negative rhomb pole at ca 20° to the mylonitic foliation pole) is favoured. These favoured crystal orientations also place one of the point maxima in the combined positive and negative acute rhomb pole figure (π and π') at an even lower angle (8°) to the foliation pole (Fig. 4).
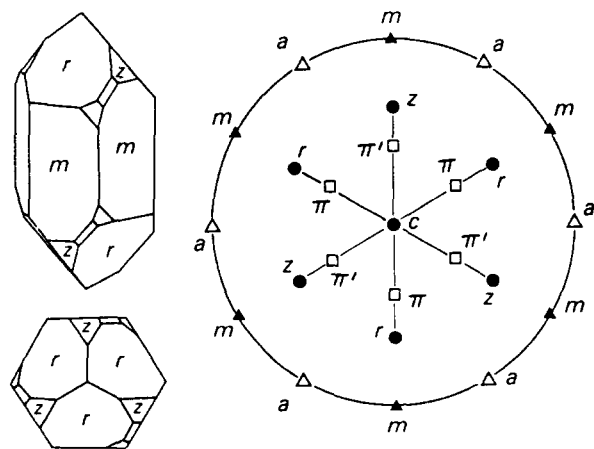
Fig. 5. Crystal faces of a quartz (adapted from Nicolas & Poirier 1976, fig. 5.26) and geometrical relationships between quartz crystallographic directions considered in this paper.

Fabric simulation studies of Lister and co-workers (e.g. Lister & Hobbs 1980) indicate that an evolving crystallographic fabric is directly related to the imposed kinematic framework and therefore, in general, bears no direct relationship with finite strain features such as foliation and lineation. Within samples from the Torridon vein, the minimum observed angle between mylonitic foliation (S_A) and the vein margins (i.e. the shear zone boundaries) was *ca* 6° (Fig. 1a). On the stereograms in Figs. 3 and 4 this would be represented by the shear zone boundaries (i.e. shear plane) being orientated such that they contain the specimen Y direction, but intersect the XZ plane at 6° from the lineation measured in a clockwise sense. The dominant *a*-axis point maximum in specimen T1 is orientated within the XZ plane at 9° to the lineation measured in a clockwise sense (Fig. 4). By analogy with the fabric simulation studies of Etchecopar (1977) this *a*-axis maximum should be orientated parallel to the bulk simple shear direction.

Following the simulation studies of Etchecopar (1977), the bulk shear plane associated with deformation of the quartz vein may be inferred to contain both the specimen Y direction and the dominant *a*-axis maximum, whilst the bulk shear direction may similarly be inferred to parallel this *a*-axis maximum (Fig. 4). For the Torridon shear zone, angular relationships between mylonitic foliation (S_A), lineation (X), recrystallized grain shape alignment (S_B), regenerated quartz *c*- and *a*-axis fabrics and the kinematic framework inferred from shear zone geometry are summarized in Fig. 6.

Note that from Fig. 6 it is clear that the inclination of S_B to the inferred bulk shear plane varies from 27 to 44°. Adopting the model for microstructural evolution within such mylonites proposed by Means (1981), Lister & Snoke (1984, figs. 11 and 12) and Knipe & Law (1987, fig. 8) it may be suggested that those elongate dynamically recrystallized quartz grains whose long axes are orientated at angles approaching 45° to the bulk shear plane have recrystallized during the last few increments of deformation preserved in this tectonite.
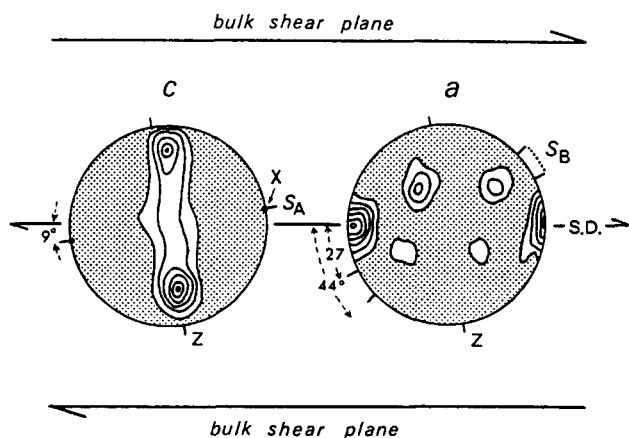
Inverse pole figures

The probability of finding a particular crystal direction aligned with a given specimen direction is expressed in the form of inverse pole figures in Fig. 7. The foliation pole is seen to favour alignment with negative forms such as the pole to the acute rhomb π' ($01\bar{1}2$—orientated at 32.5° to the *c*-axis—Frondel 1962, p. 40). The degree of preferred alignment (2.5 times uniform distribution), however, is not great (Fig. 7). Similarly, neither is there any great degree of alignment between the lineation and specific crystal directions (such as the *a*-axis). In contrast, the inferred shear plane pole point maximum (3.7 times uniform distribution) is seen to be coincident with the pole to the negative acute rhomb π'.

Interpretation of pole figure data

Slip system interpretation of the data presented in this paper follows the general approach adopted by Schmid & Casey (1986) and is based upon three fundamental assumptions:

(1) intracrystalline deformation is dominated by a single crystallographic slip system (slip plane and slip direction) within each grain (Etchecopar 1977). This

Fig. 6. Angular relationships between mylonitic foliation (S_A), pole to mylonitic foliation (Z), lineation (X), variation in oblique recrystallized quartz grain shape alignment (S_B), calculated quartz *c*- and *a*-axis fabrics and simple shear kinematic framework (bulk shear plane and shear direction—S.D.). Kinematic framework inferred from macroscopic shear zone measurements—see text for details.
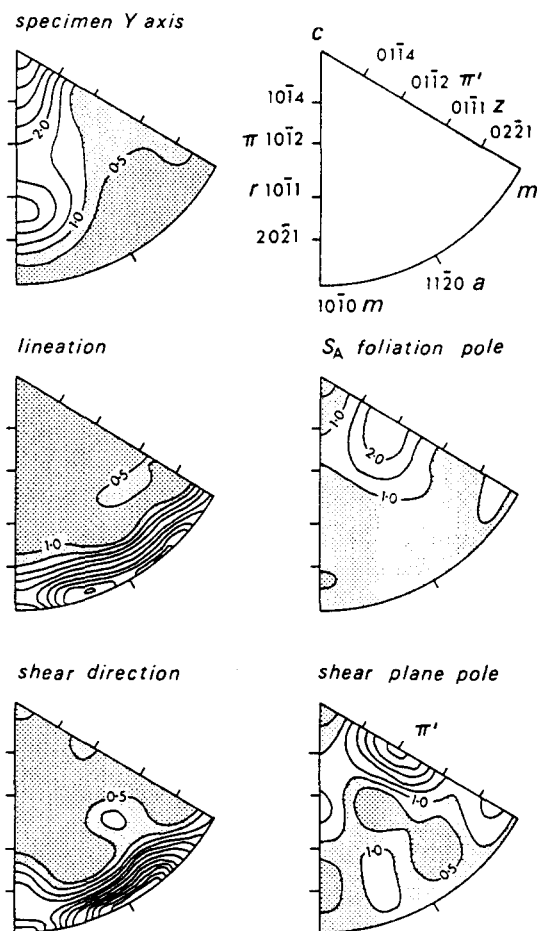

Fig. 7. Inverse pole figures calculated from the ODF for selected specimen and shear zone directions (Fig. 6). Contour intervals: 0.5, 1.0, 1.5, . . ., 5.0, 5.5, 6.0 times uniform distribution: less than 0.5 and 0.5–1.0 times uniform distribution, heavy and light stipple, respectively.

assumption does not take into account the possibility of different, simultaneously operating, slip systems within each grain (e.g. Lister *et al.* 1978);

(2) the dominant slip system within each grain becomes orientated parallel to the simple shear kinematic framework (*ideal orientations*). Thus the dominant slip plane should align with the bulk shear plane and, at very high shear strains, with the mylonitic foliation (Etchecopar 1977, Etchecopar & Vasseur 1987). Similarly the dominant slip direction should be aligned with the bulk shear direction and, at very high shear strains, the lineation;

(3) the dominant slip systems have reached *stable end orientations* and do not undergo further rotation with respect to the simple shear kinematic framework. This assumption appears to be supported by some experimental studies (e.g. Bouchez & Duval 1982, Schmid *et al.* 1987), although recent texture modelling studies for quartz (Wenk *et al.* in press) suggest that the crystal lattice may continuously rotate with respect to the kinematic framework during simple shear deformation.

Adopting these assumptions, the degree of alignment between potential crystallographic slip systems (slip plane and slip direction) and the kinematic framework may be interpreted as giving an indication of the relative activity of the various potential slip systems.

In Fig. 7 the inferred shear plane pole point maximum and pole to the negative acute rhomb π' are seen to be coincident. Making the above assumptions, this suggests that $(01\overline{1}2)$ [a] is, at least volumetrically within the aggregate of grains measured, the dominant crystallographic slip system. This inferred slip system has previously been identified (but only as a secondary slip system) from slip traces in experimental deformation of hydrolytically weakened synthetic quartz crystals (Twiss 1974, 1976, Linker *et al.* 1984, p. 4250). Within both experimentally deformed quartzites (e.g. Tullis *et al.* 1973) and natural quartz tectonites (e.g. Schmid & Casey 1986), inverse pole figure data generally indicate that intracrystalline slip is dominated by rhomb, prism and basal slip systems. Thus, the inferred dominant crystallographic slip system within the Torridon shear zone appears, in relation to other experimental and natural tectonites, to be unusual.

INDIVIDUAL 'CRYSTAL' PREFERRED ORIENTATION

In order to gain more information on the interdependence of crystallographic directions in specimen T1, 20 c-axis positions along the skeletal outline (Lister & Williams 1979) of the single c-axis girdle were selected (Fig. 8) for detailed analysis. For each c-axis position the most probable (favoured) position of: (a) poles to second- and first-order prisms (i.e. $\langle a \rangle$ and $\langle m \rangle$ directions, respectively); (b) positive and negative rhombs (r and z, respectively); and (c) positive and negative acute rhombs (π and π', respectively) were plotted on stereograms.

Background to analytical techniques

This analysis in terms of favoured crystal orientations is based on examination of a series of sections (at 10° intervals in PSI 1, PHI and PSI 2) through the three-dimensional representation of the ODF (Bunge 1981, Casey 1981). These ODF sections represent the distribution of Euler angles relating crystal axes to specimen reference axes (Euler angle convention of Casey 1981 adopted). Two such sections are presented in Fig. 8. These particular sections at PSI 1 = 80° and PSI 1 = 90° were chosen because they essentially contain all the information for crystals which position their c-axes along the single girdle c-axis fabric skeleton of specimen T1. For example, the section PSI 1 = 80° contains all the information for crystals which position their c-axes on a great-circle inclined at 10° to the 'N–S' line in a clockwise direction (i.e. on a great-circle whose pole is inclined at 80° to the 'N–S' line in a counterclockwise direction).

Representative intensity profiles (drawn parallel to PSI 2) through the ODF for selected c-axis positions are shown in Fig. 9, and the PSI 1, PHI and PSI 2 angles used to plot the favoured complete crystal orientation corresponding to two of these c-axis positions (4 and 17) are shown in Fig. 10.

Whilst the angle PSI 1 locates the great circle containing the c-axis, the angle PHI (ranging from 0 to 180°) defines the orientation of the c-axis within the great circle. At PHI = 0° and 180° the c-axis is located in the centre of the pole figure; angles ranging between PHI = 0° and 90° cover all c-axis positions in the '*northern hemisphere*', and angles between 90° and 180° covering positions in the '*southern hemisphere*' of the polar projection. The third angle, PSI 2, determines the orientation of the other crystal directions via a rotation of 0–120° (trigonal symmetry) about the final position of the c-axis.

Further details of the analytical 'single crystal' ODF techniques employed are given by Casey (1981), Schmid *et al.* (1981) and Schmid & Casey (1986).

Results of individual 'crystal' orientation analysis

From inspection of Fig. 8 it can be seen that in ODF sections PSI 1 = 80° and PSI 1 = 90° a strong intensity ridge runs parallel to the PSI 2 = 90° and 30° and PSI 2 = 80° and 40° lines, respectively, with intensity point maxima on these ridges at PHI = 65° and 125°. These intensity point maxima in the three dimensional representation of the ODF correspond with c-axis positions 4 and 17 (Fig. 9) which are, in turn, coincident with the two point maxima (7.5 and 9.9 times uniform distribution) in the c-axis fabric (Fig. 4). Intensity profiles drawn through the ODF sections (PSI 1 = 80° and PSI 1 = 90°) parallel to the PSI 2 axis for c-axis positions 4 and 17 (PHI = 65° and 125°, respectively) are shown in Fig. 9. For individual crystal c-axis positions these PSI 2 intensity profiles indicate the probability of finding other crystal directions on rotating about the c-axis.

Two peaks of unequal amplitude (trigonal character)

PSI 1 = 80°

PSI 1 = 80°

c-axis positions

120

90

60

30

0

PHI   0   30   60   90   120   150   180

PSI 2

PSI 1 = 90°

Z

Y

X

17

20

PSI 1 = 90°

120

90

60

30

0

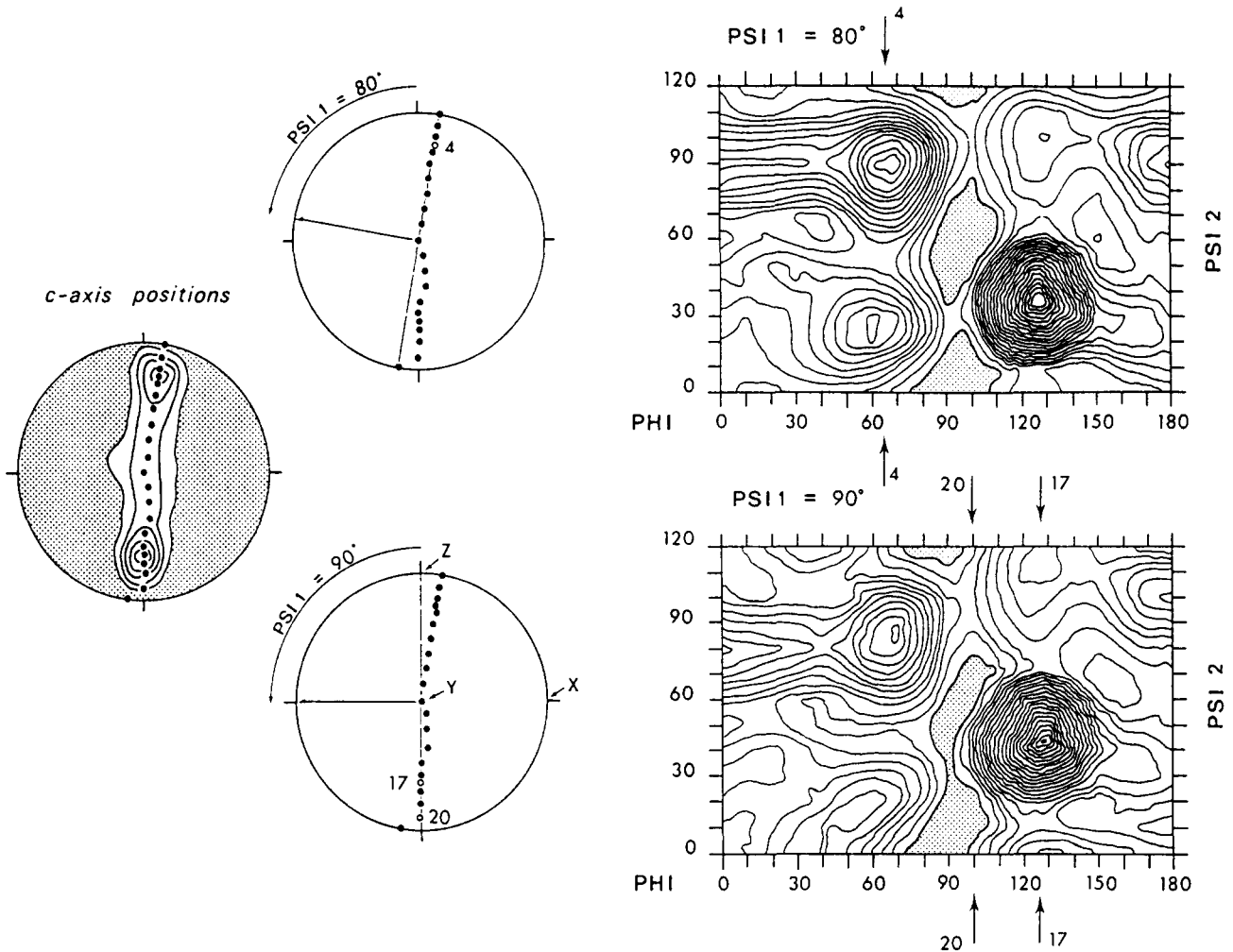PHI   0   30   60   90   120   150   180

PSI 2

20   17

Fig. 8. Selected sections (in the PSI 2 – PHI plane) through the three-dimensional representation of the ODF for specimen T1 at PSI 1 = 80° and PSI 1 = 90°. Contour intervals: 1, 2, 3, . . ., 22, 23, 24 times uniform distribution; less than uniform distribution stippled. Location on the upper-hemisphere XZ projection (displaying selected positions on the c-axis fabric skeleton) of the great circles corresponding to PSI 1 = 80° and PSI 1 = 90° are indicated. Specimen reference directions— mylonitic foliation (XY), lineation (X) and pole to mylonitic foliation (Z)—also indicated. Location of the PSI 2 intensity profiles of c-axis positions 4, 20 and 17 on the ODF sections indicated by arrows. See text for further details.
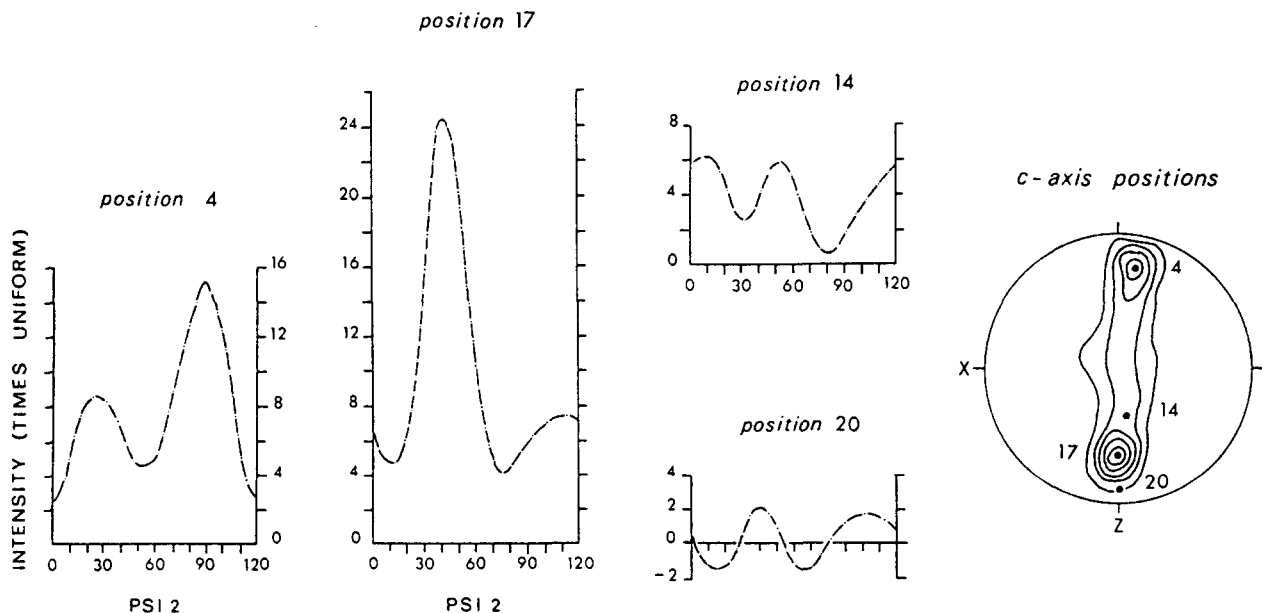
position 17

position 14

position 4

c-axis positions

24

20

16

12

8

4

0

position 20

X

4

14

17

20

Z

INTENSITY (TIMES UNIFORM)

16

12

8

4

0

0   30   60   90   120

PSI 2

0   30   60   90   120

PSI 2

8

4

0

0   30   60   90   120

4

2

0

-2

Fig. 9. PSI 2 intensity profiles through the three-dimensional representation of the ODF for specimen T1 for selected c-axis positions. *Position* 4: PSI 1 = 80°, PHI = 65°. *Position* 17: PSI 1 = 90°, PHI = 125°. *Position* 14: PSI 1 = 100°, PHI = 150°. *Position* 20: PSI 1 = 90°, PHI = 100°.
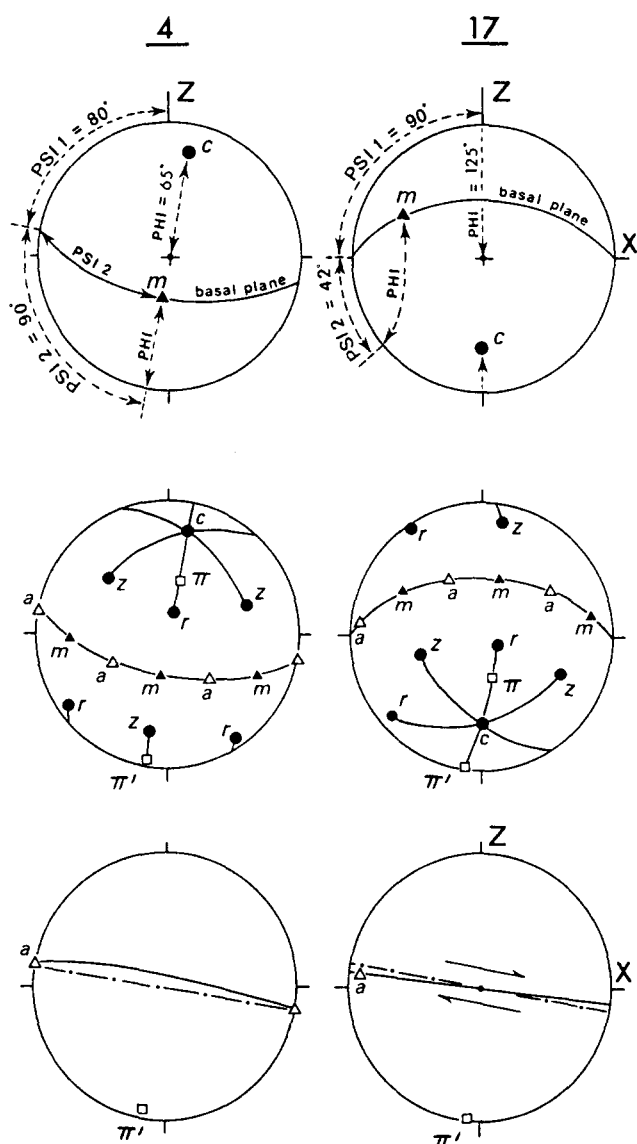
4

17

the two PSI 2 intensity peaks for position 17 is far greater than that for position 4 (Fig. 9). This contrast indicated by the ODF (Fig. 8) between strongly trigonal PSI 2 intensity profiles corresponding to c-axis positions in the 'southern hemisphere' (PHI = ca 105–145°) and more hexagonal PSI 2 intensity profiles corresponding to positions in the 'northern hemisphere' (PHI = ca 40–80°) suggests that, relative to specimen co-ordinates, the crystallographic fabric is not strictly of the monoclinic symmetry expected for such a shear zone environment.

Both c-axis (point maximum) positions 4 and 17 place a π' pole close to the foliation pole (Fig. 10); the π' poles being orientated at 6° and 3° to the inferred shear plane pole in positions 4 and 17, respectively. Crystallographic [a] directions contained within these π' planes are oriented at 0 and 10° to the inferred bulk shear direction in c-axis positions 4 and 17, respectively (cf. Figs. 6 and 10).

It should be remembered that this ODF analysis is based on X-ray data obtained by scanning over an aggregate of grains. Therefore crystal fabric intensity is proportional to the volume of grains (crystals) in that particular crystallographic orientation which have been scanned over by the X-ray beam. As there are no anomalously large grains in the aggregate scanned, it is concluded that statistically the crystallographic orientation of the majority of individual grains is such that one π' plane is placed nearly parallel to the inferred bulk shear plane, the [a] direction contained within this π' plane being orientated sub-parallel to the inferred bulk shear direction.

Favoured crystal orientations for other selected c-axis positions are shown in Fig. 11. Closest alignment between the inferred kinematic framework (Fig. 6) and potential π' [a] slip systems is found at positions 5 and 18 (7.0 and 9.0 times uniform c-axis distribution, respectively). For both these c-axis positions the π' plane is perfectly aligned with the inferred bulk shear plane. Whilst the [a] direction contained within the π' plane is perfectly aligned with the inferred bulk shear direction in position 5, that in position 18 is orientated at an angle of 10° to the shear direction (Fig. 11).

Fig. 10. Favoured crystal orientations associated with the two c-axis point maxima (positions 4 and 17) on the calculated c-axis fabric for specimen T1. All upper-hemisphere, equal-area projections viewed upwards toward the ENE. Top row: explanation of PSI 1, PHI and PSI 2 angles (measured from Figs. 8 and 9) used to construct crystal projections. Pole to mylonitic foliation indicated by Z, and lineation lying within the foliation indicated by X. See text and Casey (1981, fig. 3) for further explanation of Euler angle convention. Middle row: favoured crystal orientations for the two point maxima. Note that for clarity only the orientations of poles to positive and negative acute rhombs (π and π', respectively) located on one (of three) crystallographic zones are indicated. Bottom row: calculated orientations, for each c-axis position, of acute rhomb π' potential slip plane (solid line) most closely aligned with the bulk shear plane (broken line) inferred from shear zone geometry. Dextral shear sense indicated.

Similar high degrees of alignment between other (more commonly reported) potential slip systems and the inferred simple shear kinematic framework are found for other positions on the c-axis fabric skeleton (Fig. 11). For example, study of c-axis position 11 (4.5 times uniform c-axis distribution) indicates that individual crystals whose c-axes are aligned parallel to the specimen Y direction are perfectly orientated for prism ⟨a⟩ slip. At positions 8 and 15 (5.0 and 5.5 times uniform c-axis distribution, respectively) the ODF indicates that individual crystals are almost perfectly orientated for negative rhomb (z) ⟨a⟩ slip. These c-axis positions are located in lower intensity regions of the single girdle c-axis fabric than positions for which π' [a] potential slip planes are in alignment with the inferred kinematic framework.

are observed in the PSI 2 intensity profiles for both c-axis positions 4 and 17; these peaks are at 62° and 72° separation in positions 4 and 17, respectively (Fig. 9). Using the Euler angle convention of Casey (1981) these intensity profiles may be used to stereographically plot the favoured crystal directions associated with c-axis positions 4 and 17 (Fig. 10). Individual crystal directions (Fig. 10) associated with these two c-axis point maximum positions (4 and 17) are coincident with point maxima in the corresponding bulk specimen crystallographic fabrics (Fig. 4). The difference in amplitude of

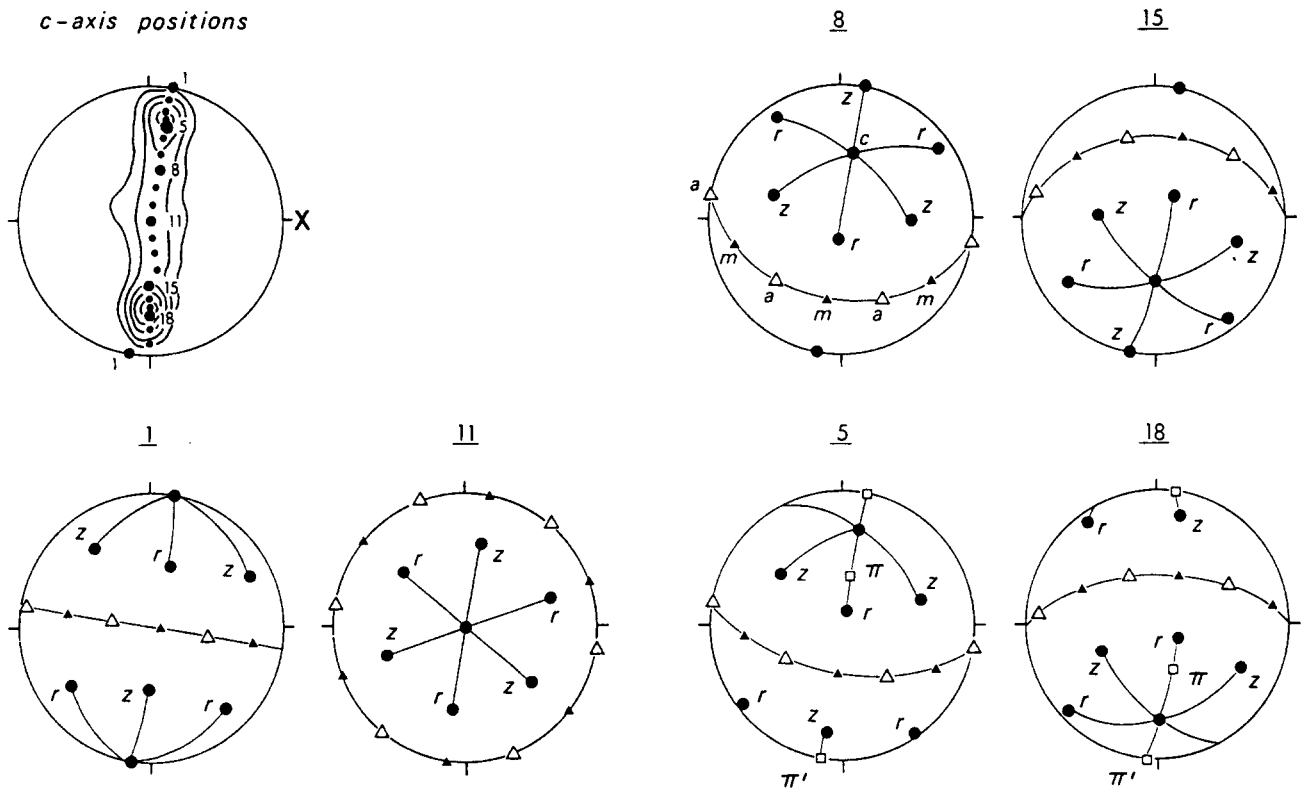This suggests that prism and rhomb slip may only be of primary importance within a relatively small number of

Fig. 11. Favoured crystal orientations associated with selected skeletal positions (numbered) on the calculated c-axis fabric for specimen T1. Note that for clarity in the stereograms corresponding to c-axis positions 5 and 18, only the orientations of poles to positive and negative acute rhombs (π and π', respectively) located on one (of three) crystallographic zones are indicated. Orientation convention as in Fig. 10. All upper-hemisphere, equal-area projections viewed upward towards the ENE.

individual grains. Similarly, although crystals in c-axis position 1 are almost perfectly orientated for basal $\langle a \rangle$ slip, the low calculated c-axis intensity (0.5 times uniform distribution) indicates that very few individual crystals (grains) are in this orientation (Fig. 11). This result is contrary to many experimentally deformed quartzites (e.g. Dell'Angelo & Tullis in press).

Relationships between individual 'crystal' orientations

Study of the ODF for specimen T1 indicates that crystals (grains) occupying different positions on the single girdle c-axis fabric skeleton are related by a common $\langle a \rangle$ direction (Fig. 12) which is coincident with the dominant a-axis point maximum (Figs. 4 and 6). Traced around the c-axis fabric skeleton the loci of the other two $\langle a \rangle$ directions define small-circles centered about this dominant (inferred bulk shear direction parallel) a-axis point maximum (cf. Figs. 6 and 12). Similarly, the loci of all three m-axes for each c-axis position, when traced from one c-axis position to the next, also define small-circle girdles centered about the dominant a-axis maximum (Fig. 12).

Therefore, as dictated by crystallography, the poles to positive (r) and negative (z) rhombs associated with individual c-axis positions must also, on being traced around the fabric skeleton, define small-circle loci centered about the dominant a-axis point maximum. In Fig. 12 we distinguish between traces of positive and negative rhombs. As one passes through the loci corresponding to

c-axis positions 14 and 20 a change over occurs in terms of preferring the positive or negative form. These two positions on the c-axis fabric skeleton are characterized by PSI 2 intensity profiles (Fig. 9) composed of two peaks of essentially equal amplitude (hexagonal character). Hence at these c-axis positions positive and negative forms are interchangeable (Fig. 13). It is interesting to note that neither of these hexagonal c-axis positions occur at PHI = 0 (c-axis parallel to Y specimen axis). Similar results have been obtained in quartz mylonites by Mancktelow (1987, p. 147) and contrast with the hexagonal character reported for Y-parallel c-axis orientations (inferred prismatic slip) by Schmid et al. (1981— specimens Gran 1 and CC 627) and Schmid & Casey (1986, p. 281—specimen PT463).

SCHMID FACTOR ANALYSIS OF POTENTIAL SLIP SYSTEMS

Schmid (1928) and Schmid & Boas (1950) have shown that for a given slip system of any orientation within a uniaxial stress field, slip begins for a given value σ_c of the shear stress resolved on the slip plane along the slip direction (Schmid's Law). This critical resolved shear stress (CRSS) is an intrinsic characteristic of each slip system, the relative CRSS values of different slip systems being controlled by directional (commonly temperature dependent) properties of the crystal lattice.

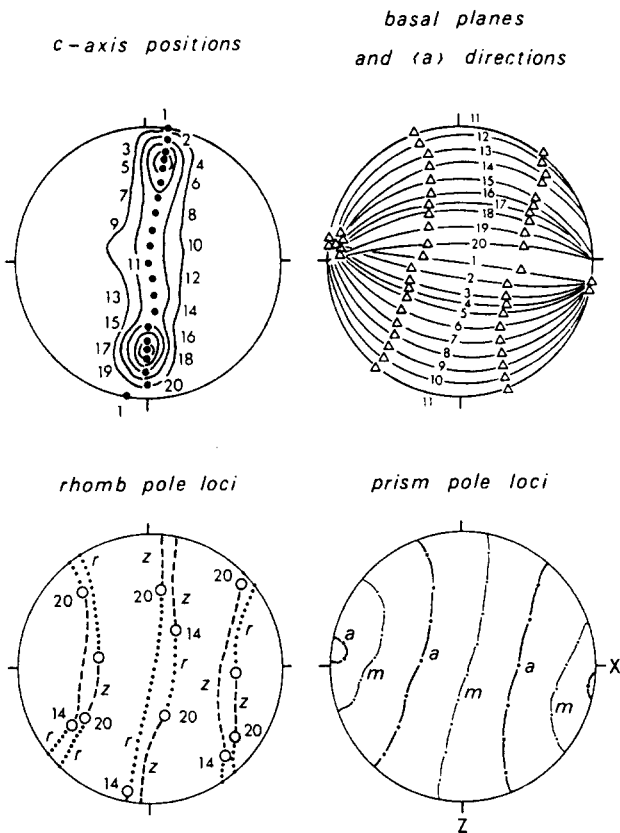It may be shown (e.g. see review by Nicolas & Poirier

c - axis positions

basal planes
and (a) directions

rhomb pole loci

prism pole loci

Fig. 12. Relationships between favoured crystal orientations corresponding to selected skeletal positions (numbered) on the calculated single-girdle c-axis fabric for specimen T1. Favoured orientations of poles to rhomb and prism planes are recorded as loci for a traverse along the c-axis fabric skeleton. Loci of poles to positive (r) rhombs represented by dotted lines, loci of poles to negative (z) rhombs indicated by broken lines. Note, that at c-axis positions 14 and 20, positive and negative forms are interchangeable (hexagonal character in the ODF). See text for further explanation. Orientation convention as in Fig. 10. All upper-hemisphere, equal-area projections viewed upwards towards the ENE.

1976, p. 40) that in a single crystalline sample subjected to uniaxial loading under an applied force F, the resolved shear stress σ_r acting on a potential crystallographic slip plane in the slip direction may be expressed by:

$$\sigma_r = \sigma_n \cdot \cos \psi \cdot \cos \lambda, \qquad (1)$$

where σ_n is the normal stress acting parallel to the applied force F, and ψ and λ are the angles the load axis makes with the slip plane normal and slip direction, respectively.

If there are several slip systems with the same CRSS, slip will begin on the system for which the resolved shear stress has the highest value for a given load F. Similarly, the relative ease of slip on otherwise identical slip systems (i.e. with the same CRSS) may be expressed by the Schmid factor S, where:

$$S = \cos \psi \cdot \cos \lambda. \qquad (2)$$

The slip system with the highest Schmid factor will be the first to be activated. It should be noted that in using equation (2), the maximum possible Schmid factor value is 0.5.
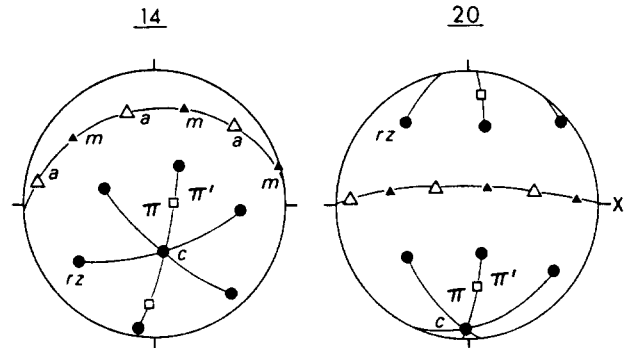
The above equations for uniaxial loading may be

14   20

Fig. 13. Favoured crystal orientations associated with the two c-axis positions (14 and 15) on the fabric skeleton at which positive and negative forms are interchangable (hexagonal character in the ODF). Note that for clarity only the orientations of poles to positive and negative acute rhombs (π and π') located on one (of three) crystallographic zones are indicated. For orientation convention see Fig. 10. Both upper-hemisphere, equal-area projections viewed upwards towards the ENE.

modified for the case of bulk simple shear (Fig. 14). For an imposed simple shear kinematic framework, it may be shown that the modified Schmid factor S_{SS} is given by:

$$S_{SS} = \cos \phi_1 \cdot \cos \alpha_3 + \cos \alpha_1 \cdot \cos \phi_3, \qquad (3)$$

where α_1 and α_3 are the angles the potential crystallographic slip plane normal makes with the bulk shear direction and shear plane normal, respectively; and ϕ_1 and ϕ_3 are the angles the potential slip direction lying
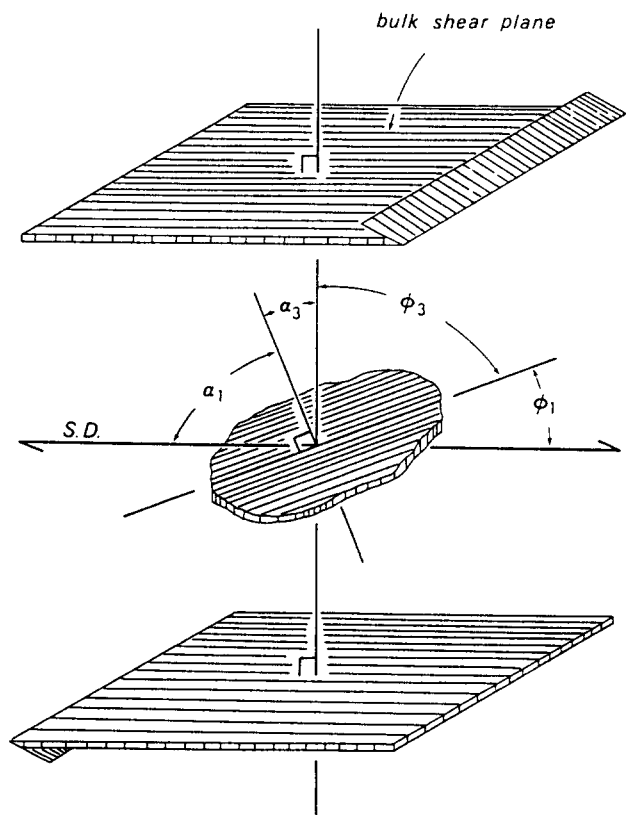
bulk shear plane

$$S_{SS} = \cos \phi_1 \cdot \cos \alpha_3 + \cos \alpha_1 \cdot \cos \phi_3$$

Fig. 14. Angular relationships between simple shear kinematic framework (bulk shear plane and shear direction—S.D.) and single crystallographic slip system (slip plane and slip direction) used to define Schmid factor (S_{SS}) for that slip system.

within the slip plane makes with the bulk shear direction and shear plane normal, respectively (Fig. 14). The derivation of this Schmid factor for simple shear is given in the Appendix. Note that if a particular slip system was perfectly aligned with the imposed kinematic framework (i.e. slip plane parallel to bulk shear plane and slip direction parallel to bulk shear direction) then, using equation (3), the Schmid factor for that particular slip system orientation would be 1.0.

Results of analysis

Using equation (3) and the ODF single 'crystal' data, modified Schmid factor values have been calculated for the potential basal, prism, rhomb (r and z) and acute rhomb (π and π') slip planes associated with the different positions on the c-axis fabric skeleton, slip in each case being in the $\langle a \rangle$ direction. In Fig. 15, these Schmid factor values for each 'crystal' orientation are plotted against their corresponding c-axis position (expressed by the angle PHI) on the fabric skeleton. This analysis assumes that: (a) the shear zone boundary is parallel to the plane of maximum shear stress; and (b) the inter-mediate principal stress is parallel to Y and equal to zero (plane stress).

Note that whilst for each c-axis position there will only be one basal $\langle a \rangle$ orientation, there will be three corresponding prism $\langle a \rangle$, six rhomb $\langle a \rangle$ (three positive and three negative) and six acute rhomb $[a]$ (three positive and three negative) orientations. Schmid factor values were calculated for each basal $\langle a \rangle$, prism (m) $\langle a \rangle$, positive rhomb (r) $\langle a \rangle$, negative rhomb (z) $\langle a \rangle$, positive acute rhomb (π) $[a]$ and negative acute rhomb (π') $[a]$ systems in which the $\langle a \rangle$ direction coincided with the dominant a-axis maximum (Figs. 4 and 6). This selective analysis of specific potential slip system orientations is based upon the premise that the shear zone reflects a two-dimensional bulk strain and that one might therefore expect the crystallographic slip directions to be oriented in the XZ specimen plane.

Schmid factor values for potential basal, prism and rhomb (r and z) $\langle a \rangle$ slip systems are shown in the top left-hand graph of Fig. 15, whilst the corresponding values for potential acute rhomb (π and π') $[a]$ systems are shown in the underlying graph.

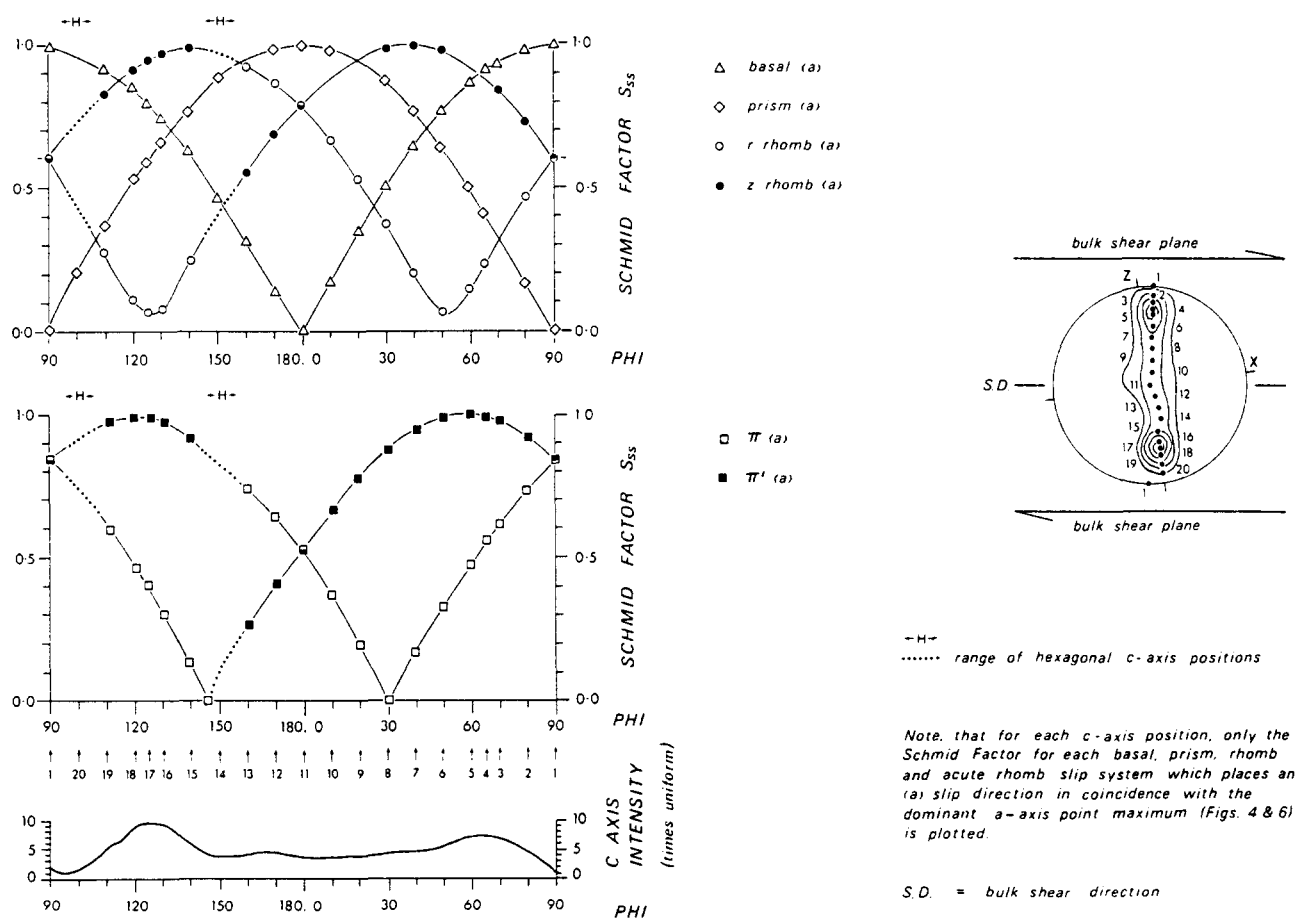All potential slip systems considered reach modified

Fig. 15. Schmid factor analysis of potential basal, prism, rhomb (r and z) and acute rhomb (π and π') $\langle a \rangle$ slip systems associated with individual positions (numbered) on the calculated c-axis fabric skeleton for specimen T1. Note obliquity between inferred simple shear kinematic framework and specimen reference directions (Z = pole to mylonitic foliation, X = lineation). For each 'single crystal' c-axis position, only the Schmid factor for each basal, prism, rhomb and acute rhomb slip system which places an $\langle a \rangle$ slip direction in coincidence with the dominant a-axis point maximum (Figs. 4 and 6) is plotted. Inclination of individual c-axes to the XZ projection plane is expressed by the angle PHI (e.g. for horizontal c-axis, PHI = 90°; for vertical c-axis, PHI = 0°, 180°). Note also correlation between Schmid factor analysis (upper and middle graphs) and corresponding intensity profile along the c-axis fabric skeleton. See text for further explanation.

Schmid factor values close to 1.0. This simply reflects the fact that the a-axis maximum closely coincides with the inferred bulk shear direction, $\langle a \rangle$ being the slip direction of all the slip systems considered. The S_{SS} values vary between 0.995 and 0.00 for basal slip, between 1.00 and 0.0 for prism slip, between 0.90–0.95 and 0.07–0.065 for rhomb slip, and finally between 1.00–0.99 and 0.00 for slip on the acute rhombs. As a consequence, all these potential slip systems are ideally orientated at certain positions along the c-axis fabric skeleton.

When the S_{SS} values are compared with the intensity profile of c-axis preferred orientation along the fabric skeleton (bottom graph in Fig. 15) one notes a close correspondence between high c-axis intensities and maxima in the S_{SS} (0.95–1.00) values for the negative acute rhombs (π') [a]. From this we infer that a very large volume portion of quartz grains give high S_{SS} values for slip on the negative acute rhombs. In addition, it should be noted (Fig. 15) that the maxima in the c-axis pole figure also coincide with c-axis positions for which one pair of basal $\langle a \rangle$ and negative rhomb $(z) \langle a \rangle$ potential slip systems have essentially equal calculated Schmid factors (approximately 0.85–0.95).

When the details of the S_{SS} curves for rhombs and acute rhombs are compared, an interesting feature emerges: the intersection points of equal S_{SS} values for the rhombs are positioned at PHI = 90 and 180°. Ideally, the range of hexagonal c-axis positions should also be positioned at these angles of PHI (Schmid & Casey 1986, p. 281). Instead they occur at PHI = 100 and 150°, as discussed earlier. In the case of curves for the acute rhombs, however, the angle PHI with a maximum S_{SS} value bisects the two ranges of hexagonal c-axis positions. No such correspondence is observed in the curves for rhomb Schmid factors. This symmetry argument additionally supports the idea that the negative acute rhombs could be the dominant slip system.

It should be noted that the graphs of Schmid factor values in Fig 15 only record (for an inferred kinematic framework) the *relative* resolved shear stresses on *potential* slip systems These graphs do not, necessarily, indicate the relative *activities* of the potential slip systems for each c-axis position. This is because activity depends both on the Schmid factor and the CRSS (Nicolas & Poirer 1976, p. 42). However, it can be argued that minimum strain energy expenditure is reached when the slip system with the highest probability to have a high Schmid factor for a majority of grains has a low CRSS value at the same time. Based on this argument it could be inferred that if the acute rhomb (π') [a] slip system (associated with the c-axis point maxima) had a low CRSS, then it may have had the highest activity. It has previously been noted, however, that in hydrolytically weakened synthetic quartz crystals (e.g. Twiss 1974) the acute rhomb (π) [a] system has only been associated with secondary slip. From Fig. 15 it is clear that these c-axis maxima positions with high (π') [a] calculated Schmid factor values (0.95–1.00) are also characterized by only slightly lower Schmid factor values (0.85–0.95) for one pair of potential basal $\langle a \rangle$ and negative rhomb $(z) \langle a \rangle$ slip

systems. This could be interpreted as indicating a high activity on simultaneously operating basal $\langle a \rangle$ and negative rhomb $(z) \langle a \rangle$ slip systems.

Preferred orientation of positive and negative crystallographic forms

The ODF for specimen T1 clearly indicates that positive and negative crystallographic forms are not equivalent (Figs. 4 and 7). Thus, for example, analysis of single 'crystal' orientations indicates that peak Schmid factor values are always associated with negative rhomb (z) and acute rhomb (π') potential slip systems (Fig. 15). These observations could be interpreted as indicating that resistance to slip is lower on negative than on positive forms.

Alternatively, it could be argued that the non-equivalence of positive and negative forms is related to Dauphiné twinning rather than orientation controlling slip mechanisms. This Dauphiné twinning could have acted upon an aggregate of grains (originally characterized by equivalent pole figures for forms such as r and z) in which there was equal resistance to slip on positive and negative forms. This Dauphiné twinning could have occurred either during or after the main intracrystalline deformation.

A Dauphiné twin is related to its host by a 180° rotation about the c-axis. In such twinning the crystal axes remain parallel, but the polarity of the a-axis is reversed; thus a positive trigonal form, such as r, is exchanged for a negative form, such as z, and vice versa. For experimental axially symmetric flattening. Tullis & Tullis (1972) were able to demonstrate from inverse pole figure data that Dauphiné twinning resulted in a depletion of compression axes near the z rhomb poles and an augmenting of them near r. Thus solely on the basis of the rhomb pole figure data in Fig. 4, it could be argued that the non-equivalence between the r and z pole figures is due to uniaxial compression parallel to the 'NW–SE-trending' positive (r) point maximum contained within the XZ plane (Fig. 4). This r point maximum is orientated at 35° to the foliation pole (Fig. 4) and is sub-parallel to the maximum principal compression direction associated with the inferred simple shear kinematic framework (Fig. 6).

With the information available it is difficult to decide between these two interpretations. However, it is suggested that the elegantly simple detected relationships between, for example, c-axis orientations associated with maximum Schmid factor values for negative acute rhomb (π') [a] systems and c-axis positions associated with hexagonal (change over) positions (Fig. 15) may be most easily explained in terms of crystallographic slip. It is, therefore, proposed that such relationships may indicate that the crystallographic fabric has formed in response to a single and internally consistent mechanism of fabric formation, rather than by the superimposition of fabric elements caused by glide with other elements caused by Dauphiné twinning.

CONCLUSIONS

Integration of shear zone geometry measurements with microstructural and crystallographic fabric analysis of the mylonitic quartz-rich *L–S* tectonite (specimen T1) from the Torridon shear zone described in this paper leads to the following conclusions.

(1) The crystallographic fabric is characterized by a dominant *a*-axis point maximum lying within the *XZ* plane and orientated at 9° to the lineation; this *a*-axis point maximum occupies a pole position to the corresponding single girdle *c*-axis fabric. ODF analysis indicates that individual positions on the *c*-axis fabric skeleton are related by a common $\langle a \rangle$ direction which is coincident with this dominant *a*-axis point maximum.

(2) The dominant *a*-axis maximum is, within observational error, orientated sub-parallel to the bulk shear direction indicated by shear zone geometry.

(3) An elegantly simple set of relationships was found between shear zone geometry and the orientation of potential slip systems associated with individual 'crystals' occupying different positions on the *c*-axis fabric skeleton.

(4) Both inverse pole figure data and Schmid factor analysis of potential slip system orientations indicate that, within the majority of quartz grains measured, one potential acute negative rhomb (π') $[a]$ slip system in each 'grain' is almost perfectly aligned with the inferred simple shear kinematic framework. This strong alignment could be interpreted as indicating the importance of acute rhomb $[a]$ slip in this particular tectonite, although the possibility of simultaneously operating basal $\langle a \rangle$ and negative rhomb (z) $\langle a \rangle$ slip is also indicated by the Schmid factor data.

Crystallographic fabrics from specimen T1 may easily be interpreted in terms of the simple shear kinematic framework indicated by the shear zone geometry. These results are essentially in agreement with the fabric evolution model proposed by Etchecopar (1977) for bulk simple shear deformation.

Thus, at least in this particular geometrically closely constrained geological example, the crystallographic fabrics strongly support the bulk simple shear kinematic framework indicated by shear zone geometry. This qualified statement does not, however, justify making an *a priori assumption* that the formation of all mylonite zones is due to strict simple shear deformation. Interpretation of individual deformation zones must be made on the basis of all locally available information, rather than on general structural models.

REFERENCES

Bouchez, J.-L. 1978. Preferred orientations of quartz *a*-axes in some tectonites: kinematic inferences. *Tectonophysics* **49**, T25–T30.

Bouchez, J.-L., Dervin, P., Mardon, J. P. & Englander, M. 1979. La diffraction neutronique appliquée à l'étude de l'orientation préférentielle de réseau dans les quartzites. *Bull. Mineral.* **102**, 231–255.

Bouchez, J.-L. & Duval, P. 1982. The fabric of polycrystalline ice deformed in simple shear: experiments in torsion, natural deformation and geometrical interpretation. *J. Textures & Microstruct.* **5**, 1–17.

Bouchez, J.-L., Lister, G. S. & Nicolas, A. 1983. Fabric asymmetry and shear sense in movement zones. *Geol. Rdsch.* **72**, 401–419.

Bunge, H. J. 1981. Fabric analysis by Orientation Distribution Functions. *Tectonophysics* **78**, 1–21.

Burg, J.-P. & Laurent, P. 1978. Strain analysis of a shear zone in a granodiorite. *Tectonophysics* **47**, 15–42.

Casey, M. 1981. Numerical analysis of X-ray texture data: an implementation in FORTRAN allowing triclinic or axial specimen symmetry and most crystal symmetries. *Tectonophysics* **78**, 51–64.

Dell'Angelo, L. N. & Tullis, J. In press. Fabric development in experimentally sheared quartzites. *Tectonophysics*.

Etchecopar, A. 1977. A plane kinematic model of progressive deformation in a polycrystalline aggregate. *Tectonophysics* **39**, 121–139.

Etchecopar, A. & Vasseur, G. 1987. A 3.D kinematic model of fabric development in polycrystalline aggregates: comparisons with experimental and natural examples. *J. Struct. Geol.* **9**, 705–718.

Frondel, C. 1962. *Dana's System of Mineralogy, Vol. 3, Silica Minerals*. John Wiley, New York.

Hobbs, B. E. 1985. The geological significance of microfabric analysis. In: *Preferred Orientations in Deformed Metals and Rocks* (edited by Wenk, H.-R.). Academic Press, New York, 463–484.

Knipe, R. J. & Law, R. D. 1987. The influence of crystallographic orientation and grain boundary migration on microstructural and textural evolution in a *S–C* mylonite. *Tectonophysics* **135**, 155–169.

Law, R. D. 1987. Heterogeneous deformation and quartz crystallographic fabric transitions: natural examples from the Moine thrust zone at the Stack of Glencoul, northern Assynt. *J. Struct. Geol.* **9**, 819–833.

Law, R. D., Casey, M. & Knipe, R. J. 1986. Kinematic and tectonic significance of microstructures and crystallographic fabrics within quartz mylonites from the Assynt and Eriboll regions of the Moine thrust zone, NW Scotland. *Trans. R. Soc. Edinb., Earth Sci.* **77**, 99–126.

Law, R. D., Knipe, R. J. & Dayan, H. 1984. Strain path partitioning within thrust sheets: microstructural and petrofabric evidence from the Moine thrust zone at Loch Eriboll, northwest Scotland. *J. Struct. Geol.* **6**, 477–497.

Linker, M. F., Kirby, S. H., Ord, A. & Christie, J. M. 1984. Effects of compression direction on the plasticity and rheology of hydrolytically weakened synthetic quartz crystals at atmospheric pressure. *J. geophys. Res.* **89**, 4241–4255.

Lister, G. S. & Hobbs, B. E. 1980. The simulation of fabric development during plastic deformation, the effects of deformation history. *J. Struct. Geol.* **2**, 35–370.

Lister, G. S. & Paterson, M. S. 1979. The simulation of fabric development during plastic deformation and its application to quartzites: fabric transitions. *J. Struct. Geol.* **1**, 283–297.

Lister, G. S., Paterson, M. S. & Hobbs, B. E. 1978. The simulation of fabric development in plastic deformation and its application to quartzites: the model. *Tectonophysics* **45**, 107–158.

Lister, G. S. & Snoke, A. 1984. S–C mylonites. *J. Struct. Geol.* **6**, 617–638.

Lister, G. & Williams, P. F. 1979. Fabric development in shear zones, theoretical controls and observed phenomena. *J. Struct. Geol.* **1**, 283–297.

Mancktelow, N. S. 1987. Quartz textures from the Simplon Fault Zone, southwest Switzerland and north Italy. *Tectonophysics* **135**, 133–153.

Means, W. D. 1981. The concept of steady-state foliation. *Tectonophysics* **78**, 179–199.

Nicolas, A. & Poirier, J. P. 1976. *Crystalline Plasticity and Solid State Flow in Metamorphic Rocks*. John Wiley, London.

Platt, J. P. & Behrmann, J. H. 1986. Structures and fabrics in a crustal

scale shear zone, Betic Cordilleras, SE Spain. *J. Struct. Geol.* **8**, 15–34.

Ramsay, J. G. 1980. Shear zone geometry: a review. *J. Struct. Geol.* **2**, 83–100.

Ramsay, J. G. & Graham, R. H. 1970. Strain variation in shear belts. *Can. J. Earth Sci.* **7**, 786–813.

Schmid, E. 1928. Zn normal stress law. *Proc. Int. Congr. Appl. Mech*, Delft, 342.

Schmid, E. & Boas. W. 1950. *Plasticity of Crystals.* F. A. Hughes, London.

Schmid, S. M. 1982. Microfabric studies as indicators of deformation mechansims and flow laws operative in mountain building. In: *Mountain Building Processes* (edited by Hsu, K. J.). Academic Press, London, 95–110.

Schmid, S. M. & Casey, M. 1986. Complete fabric analysis of some commonly observed quartz c-axis patterns. In: *Mineral and Rock Deformation; Laboratory Studies—The Paterson Volume* (edited by Hobbs, B. E. & Heard, H. C.). *Am. Geophys. Un. Geophys. Monogr.* **36**, 263–286.

Schmid, S. M., Casey, M. & Starkey, J. 1981. An illustration of the advantages of a complete texture analysis described by the Orientation Distribution Function (ODF) using quartz pole figure data. *Tectonophysics* **78**, 101–117.

Schmid, S. M., Panozzo, R. & Bauer, S. 1987. Simple shear experiments on calcite rocks: rheology and microfabric. *J. Struct. Geol.* **9**, 747–778.

Simpson, C. 1981. Ductile shear zones: a mechanism of rock deformation in the orthogneisses of the Maggia Nappe, Ticino. Unpublished Ph.D thesis, ETH, Zurich.

Takeshita, T. & Wenk, H.-R. 1988. Plastic anisotropy and geometrical hardening in quartzites. *Tectonophysics* **149**, 345–361.

Tullis, J., Christie, J. M. & Griggs, D. T. 1973. Microstructures and preferred orientations of experimentally deformed quartzites. *Bull. geol. Soc. Am.* **84**, 297–314.

Tullis, J. & Tullis, T. E. 1972. Preferred orientation produced by mechanical Dauphiné twinning: thermodynamics and axial experiments. In: *Flow and Fracture of Rocks* (edited by Heard, H. C., Borg, I., Carter, N. & Raleigh, C.). *Am. Geophys. Un. Geophys. Monogr.* **16**, 67–82.

Twiss, R. J. 1974. Structure and significance of planar deformation features in synthetic quartz. *Geology* **2**, 329–332.

Twiss, R. J. 1976. Some planar deformation features, slip systems, and submicroscopic structures in synthetic quartz. *J. Geol.* **84**, 701–724.

Wenk, H.-R., Canova, G., Molinari, A. & Kocks, U. F. In press. Viscoplastic modeling of texture development in quartzite. *J. geophys. Res.*

Wheeler, J. 1986. Physical and chemical processes in ductile shear zones. Unpublished Ph.D thesis, University of Leeds.

APPENDIX

DERIVATION OF SCHMID FACTOR FOR SIMPLE SHEAR

Suppose we have a crystal in a stress regime whose stress tensor is σ. Then the stress vector acting on a plane, whose unit vector normal is n, is

$$v = \sigma n \tag{A1}$$

and the shear component resolved parallel to a potential shear direction d is

$$\sigma_R = d \cdot v = d \cdot \sigma n. \tag{A2}$$

The Schmid factor we use is a normalized version of this, in which the maximum possible shear stress in a given stress system is normalized to 1:

$$S = \sigma_R/\sigma_R(\max). \tag{A3}$$

Equation (A3) applies to any stress system, and from it the Schmid factor for uniaxial loading may be derived as a special case. To derive S for a simple shear zone, the bulk stress tensor is required. Simple shear is defined geometrically, so a constitutive flow law may be used to obtain the stress tensor. In a material undergoing power-law creep, the flow law is

$$\sigma = Pg + 2f(\sigma)\dot{e}, \tag{A4}$$

where g is the unit tensor, P represents the hydrostatic part of the stress, $\dot{e}$ is the strain rate tensor and $f(\sigma)$ is a function of stress expressing the power-law dependence. In a simple shear zone, where $\dot{\gamma}$ is the shear strain rate,

$$\dot{e} = 1/2 \begin{bmatrix} 0 & 0 & \dot{\gamma} \\ 0 & 0 & 0 \\ \dot{\gamma} & 0 & 0 \end{bmatrix} \tag{A5}$$

so

$$\sigma = \begin{bmatrix} P & 0 & f\dot{\gamma} \\ 0 & P & 0 \\ f\dot{\gamma} & 0 & P \end{bmatrix}. \tag{A6}$$

The maximum and minimum principal stresses are at 45° to the shear zone plane and movement direction. If we express n in terms of the angles α_i it makes with the co-ordinate axes, and d in terms of angles ϕ_i with each axis (Fig. 14), then from (A2) and (A6)

$$\sigma_R = f\dot{\gamma}(\cos\phi_1 \cdot \cos\alpha_3 + \cos\alpha_1 \cdot \cos\phi_3).$$

Note all terms in P have disappeared because d and n are orthogonal. The normalized version of this resolved shear stress is the Schmid factor for simple shear,

$$S_{SS} = \cos\phi_1 \cdot \cos\alpha_3 + \cos\alpha_1 \cdot \cos\phi_3.$$